fluids

Article

Unsteady Modelling of the Mixing Efficiency, Species Transport, and Flow Structure in a Novel Photochemical Reactor

Zakaria Mansouri [1,*], Richard Jefferson-Loveday [2], Stephen J. Pickering [3] and Michael W. George [4]

[1] Department of Engineering, Nottingham Trent University, Nottingham NG11 8NS, UK
[2] Engineering Department, King's College London, Strand, London WC2R 2LS, UK
[3] Department of Mechanical, Materials and Manufacturing Engineering, University of Nottingham, University Park, Nottingham NG7 2RD, UK
[4] School of Chemistry, University of Nottingham, University Park, Nottingham NG7 2RD, UK
* Correspondence: zak.mansouri@ntu.ac.uk

Abstract

This paper deals with computational fluid dynamics (CFD) to improve the design of a new scalable photochemical reactor which uses the Taylor–Couette flow principle. This study aims to investigate the ways to improve the mixing efficiency (M_{eff}) within the reactor, as it is a key parameter to increase the productivity and inform the future scale-up of the novel reactor. The investigated design parameters are the gap size (d) between the reactor cylinders, the rotational speed (Ω) of the inner cylinder, the flow rate of the reagent ($\dot{V}$), and the dynamic viscosity of the mixture (μ). For all the investigated cases, the results show that the temporal evolution of the M_{eff} increases and then becomes steady after a maximum level is reached. The point of the maximum M_{eff} is called the equilibration time. It is revealed that the M_{eff} is mainly affected by the flow rate increase as it contracts the Taylor vortices and consequently the mixing deteriorates.

Keywords: CFD; Taylor flow; photochemical reactor; mixing efficiency; reactor design

1. Introduction

The flow between two concentric cylinders with the inner cylinder rotating is known as Taylor–Couette flow and has been studied for many decades (since Taylor's experiments in 1923 [1]). In the early studies, it was found that the flow exhibits an instability when the rotation speed exceeds a critical value. Pairs of counter-rotating vortices are formed and distributed regularly along the cylinder gap axis due to the shear force, as illustrated in Figure 1. The rotational Reynolds number, known also as the Taylor number, is used to indicate the flow regime and its transition from Couette flow (flow without vortices) to Taylor flow. The Taylor number is defined as $Ta = \rho U_{\Omega} d/\mu$, where ρ is the density of the fluid, U_{Ω} is the linear speed of the inner cylinder, $d = R_o - R_i$ is the gap width, R_o is the outer cylinder radius, R_i is the inner cylinder radius, and μ is the dynamic viscosity of the fluid. Di Prima and Swinney [2] reported that the continuous increase in Taylor number leads to the appearance of three new flow regimes, which are the wavy Taylor flow, the random Taylor flow, and the turbulent Taylor flow. The initial Taylor flow and the wavy Taylor flow are both laminar and the random Taylor flow is transitional. Based on many previous experimental investigations, Di Prima and Swinney [2] also reported that the critical Taylor numbers that indicate the transition from one regime to another depend on the radius ratio of the cylinders $\eta = R_i/R_o$. For example, Figure 2 shows the relationship between the critical Taylor number of the first transition (from Couette to Taylor flow) and

Check for updates

Academic Editor: Chandrashekhar S. Jog

Received: 9 December 2025
Revised: 16 January 2026
Accepted: 2 February 2026
Published: 5 February 2026

https://doi.org/10.3390/fluids11020045

the radius ratio η = [0.1–0.975]. It can be seen that the increase in the radius ratio promotes a rapid transition to the first instability regime. This is due to the tightening of the annular gap, where the cylinders' walls become closer to each other and generate more shear force. One can also note that the experimental points can be represented by a power law function, which simplifies the prediction of the critical Taylor number.

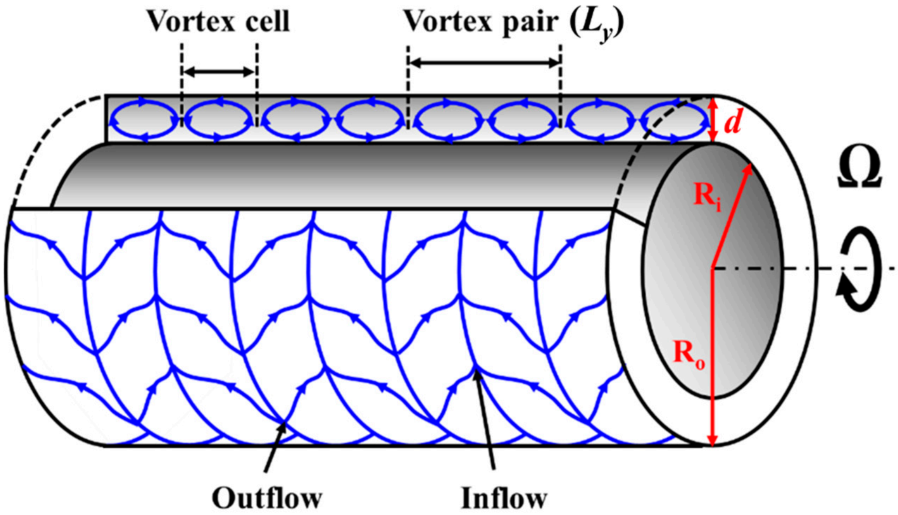

Figure 1. Schematic of the vortex structure of Taylor–Couette flow.

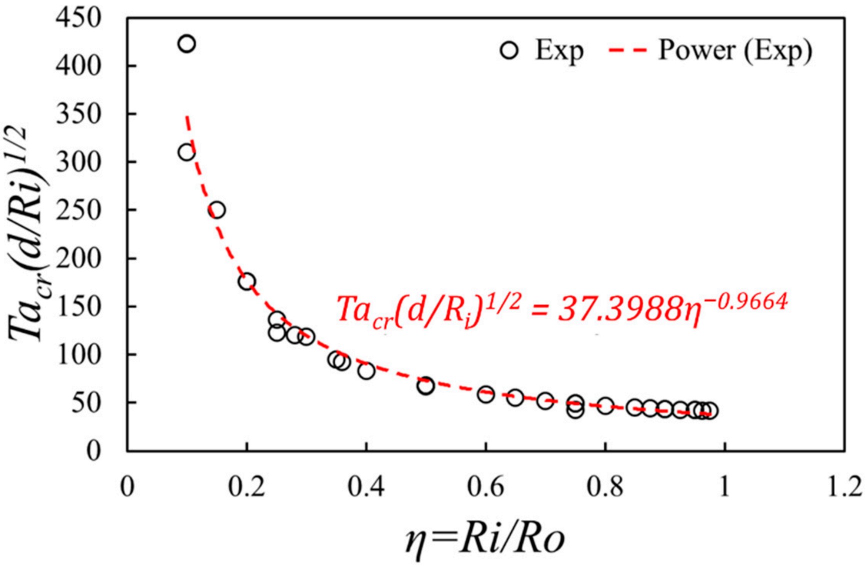

Figure 2. Experimental critical values of Taylor number for different values of the radius ratio according to Di Prima and Swinney [2].

The early experiments that led to the identification of the different instabilities and critical transition numbers used visual observations to draw their conclusions. Subsequent investigations from the 1970s to the 1990s used flow velocity measurement instruments, such as hot-wire anemometry and laser Doppler velocimetry (LDV) to measure velocity components at a series of points within the annular gap [3–5]. For example, Simmers and Coney [3] employed the hot-wire anemometry technique on a Taylor–Couette configuration and obtained axial, tangential, and radial velocity profiles within the annular gap. Heinrichs et al. [4] used LDV to measure the axial velocity in Taylor vortex flow at a fixed radial position for a series of points distributed along the axial direction. Takeda et al. [5] used an ultrasonic Doppler velocity technique to measure the one-dimensional unsteady axial velocity in a wavy Taylor flow. All these experimental investigations were conducted to support the flow regimes previously observed by visual observations and to quantify the flow velocity at each regime. In recent years, more sophisticated measurement techniques have been employed, such as the particle image velocimetry (PIV) to obtain two-dimensional contours of the flow velocity over meridional or cross azimuthal planes [6–9] in order to provide more detailed information about the nature of the vortices. Wereley and Lueptow [6] used PIV to measure the axial and radial velocities and visualise the flow in a meridional plane over an annular gap for laminar Taylor and wavy Taylor flows. For the laminar Taylor flow, their results showed that, as the Taylor number increases, the vortices become stronger and the outflow between the vortex pairs becomes jet-like. For the wavy Taylor case, the flow was characterised by azimuthally wavy deformation of the vortices, both axially and radially. Nemri et al. [7] coupled PIV and planar laser-induced fluorescence (PLIF) to measure the mixing properties of different flow regimes and their effect on the dispersion of a passive tracer. The findings showed that lower azimuthal wavenumbers and longer axial wavelengths result in larger axial dispersion.

Computational fluid dynamics (CFD) of Taylor–Couette flow has provided detailed information about the velocity field, flow behaviour, shear characteristics, and other transport features [10–16]. In the recent years, many CFD techniques for turbulence prediction, such as Reynolds-averaged Navier–Stokes (RANS) modelling [11,12], large eddy simulation (LES) [13,14], and direct numerical simulation (DNS) [7,15] have been used to interrogate the different flow regimes. Li et al. [12] conducted a numerical study using the Reynolds stress model (RSM) to investigate the flow in a Taylor–Couette configuration with variable cross section inner cylinders. This approach was used to obtain a variable annular gap width that effects the flow vortices and shear forces applied on the cylinders. Results showed that the regions of low shear rate are effectively reduced in the modified design compared to the original design. Taylor vortices formed in the gap became temporal–periodic with respect to the outer cylinder. Cheng et al. [14] performed an LES study on turbulent Taylor flow configurations of $\eta = 0.909$ for a range of Taylor number $Ta = [10^5–10^6]$. The authors derived an empirical model from the numerical results, which can accurately predict the wall-layer thickness.

In practical applications, Taylor–Couette flow has shown great potential. The toroidal motion of the fluid elements within the vortices promotes highly efficient radial mixing [16] and heat transfer improvement [17]. Thus, each vortex cell can be regarded as a well-mixed small batch reactor. If an axial flow is added, the Taylor–Couette flow configuration enables converting the small batch reactors to a big continuous reactor. Nowadays, continuous Taylor–Couette flow is widely used in process engineering (e.g., substance separation [18] and particles preparation [19]), bio engineering (e.g., bioreactors [20]), and chemical engineering (photochemical reactors [21,22] and electrochemical reactors [23,24]).

Lee et al. [21] developed a new photo-oxidation continuous reactor using the Taylor–Couette flow principle and light source (e.g., visible light or UV light). The reactor is called a photo-vortex reactor and it contains a bore forming a duct inside the rotating cylinder to add gases into the annular gap. This technique presents many advantages for reactions with added gases (e.g., air and oxygen). They found that the rapid mixing generated by the vortices enabled rapid mass transfer between the gas and the liquid, allowing for a high-efficiency dissolution of gases. Later, Lee et al. [22] scaled up the photo-vortex reactor to increase the productivity of the chemical compound from grams to kilos per day. The authors proved that the photochemistry combined with Taylor–Couette flow can be scalable and achieved an increase in productivity of over 300 times.

In view of the scarcity of works concerning the CFD modelling of photochemical Taylor–Couette reactors used for flow chemistry, the main aim of the present study is to investigate the design parameters affecting the mixing that are key for reactor productivity. In addition, the transport behaviour of chemical reactants under the coupling of Taylor–Couette flow and axial flow has not been investigated previously in the literature. The present study will reveal the unsteady species transport behaviour affected by the flow structures of the Taylor–Couette principle combined with an axial flow. The studied configuration is the experimental photo-vortex reactor under continuous development [21,22], which has not been investigated numerically before. A numerical parametric study will be conducted using unsteady Reynolds average Navier–Stokes (URANS) modelling with the Wilcox k-ω model for turbulence closure. Four main design parameters will be investigated, which are the annular gap size (width), the rotation speed of the inner cylinder, the flow rate, and the fluid viscosity. The mixing efficiency at the unsteady start-up phase will be reported for the different design parameters, which is a measure of how the toroidal motion of the vortices is contributing the conversion and transport of the chemical reagents until a steady state is reached. The flow structure and species distribution will be discussed in detail as well.

2. Taylor Vortex Reactor Configuration

The photochemical reactor adopted in this work was developed by Lee et al. [21,22] to investigate the scalability and productivity of organic chemical compounds. It is a continuous flow reactor that uses the Taylor–Couette flow principle. Figure 3a shows a photograph of the deconstructed test-rig of the reactor, and Figure 3b shows a schematic representation of the reactor. This version of photo-vortex reactor has a length L = 190 mm and consists of a transparent Pyrex jacketed tube that is sealed at the bottom. The jacket diameter is D_j = 40 mm, and the Pyrex tube diameter is D_o = 22 mm. The reactor contains a rotating stainless-steel cylinder (inner cylinder) with a narrow bore forming a coaxial duct (central duct) through its centre to allow the delivery of the reactants. The diameter of the rotating cylinder is D_i = 10 mm and can be changed to adjust the gap width between it and the Pyrex tube. The reactor has a vertical orientation such that the light source (e.g., LED blocks) can be more easily arranged around the outside. The rotation of the inner cylinder is provided by an electric motor using a drive belt and both are located next to the reactor. The rotating cylinder is fixed on bearings inside an aluminium block to eliminate vibrations and allow free rotation at high speed. During operation and for safety reasons, the moving parts (e.g., the motor, the drive belt, the bearings, and the top of the inner cylinder) are housed inside an aluminium case. The rotation speed (Ω) can be adjusted gradually from 50 rpm to 4000 rpm by a control box connected to the motor. To deliver the reactants into the reactor, the central duct of the rotating cylinder is attached to a stationary tube that connects to a HPLC pump. The jacketed Pyrex tube broadens out into an upper plenum to allow the reagent solution to exit the annual gap. The plenum is connected to a peristaltic pump, where its flow rate is adjusted to suit the reagent exit flow rate. The reactor can operate with different light sources (e.g., visible light or UV light). In Figure 3a, around the reactor sit three LED blocks located at 50 mm. The Pyrex jacket and the LEDs are connected to a cooling system to ensure that the reactor temperature is constant by removing the heat generated by the LEDs.

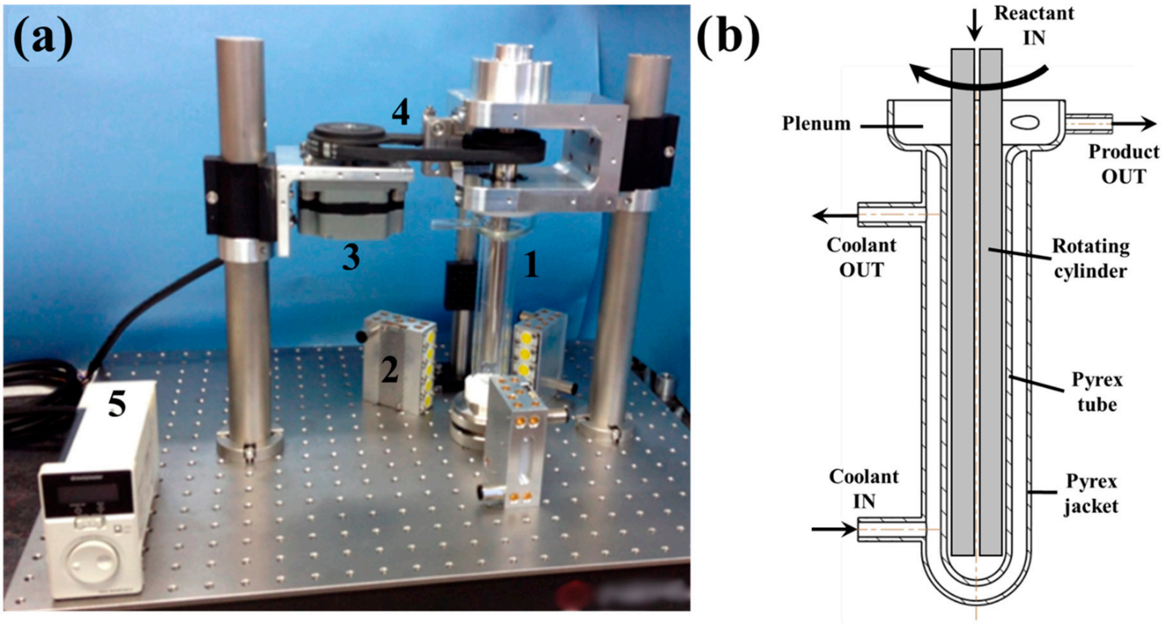

Figure 3. (**a**) Photograph of the deconstructed reactor test-rig with (1) the photo-vortex reactor, (2) LEDs, (3) electric motor, (4) drive belt, and (5) control box [22]. (**b**) Schematic of the photo-vortex reactor showing the feeding and removal of reagents and coolant.

3. Numerical Setup

3.1. Solver and Governing Equations

Unsteady incompressible simulations of the photo-vortex reactor were conducted using the ANSYS-Fluent 2022R1 CFD solver. It is a Navier–Stokes solver, which uses the finite volume method for the spatial discretisation, and it can handle both 2D and 3D flow problems. The second-order upwind scheme was selected for the spatial discretisation. The second-order implicit scheme was used for the time discretisation. The solved equations for both laminar and turbulent regimes are (1) the mass conservation, (2) flow momentum, and (3) species transport.

$$\nabla \cdot \mathbf{u} = 0 \tag{1}$$

$$\frac{\partial \mathbf{u}}{\partial t} + (\mathbf{u} \cdot \nabla)\mathbf{u} = -\frac{1}{\rho}\nabla p + \nu \nabla^2 \mathbf{u} + \mathbf{g} \tag{2}$$

where $\mathbf{u}$, ρ, p, ν, and $\mathbf{g}$ denote velocity, density, pressure, kinematic viscosity of the fluid, and gravity, respectively. The gravity $\mathbf{g} = -\nabla(gx) = (0, 0, -g)$ with x is the vertical coordinate, as shown in Figure 5 of Section 3.3. The velocity $\mathbf{u}$ is decomposed as the sum of an average velocity U_i and a fluctuating velocity u_i'.

$$\frac{\partial Y_i}{\partial t} + \nabla \cdot (\mathbf{u} Y_i) = -\frac{1}{\rho} \nabla \cdot J_i \tag{3}$$

where Y_i and J_i are the mass fraction and diffusion flux of the species i.

The turbulence was handled using the k-ω model [25], where two extra equations are solved: the turbulent kinetic energy (k),

$$\frac{\partial k}{\partial t} + U_j \frac{\partial k}{\partial x_j} = \tau_{ij} \frac{\partial U_i}{\partial x_j} - \beta^* k \omega + \frac{\partial}{\partial x_j}\left[(\nu + \sigma^* \nu_t) \frac{\partial k}{\partial x_j} \right] \tag{4}$$

and the specific dissipation rate (ω).

$$\frac{\partial \omega}{\partial t} + U_j \frac{\partial \omega}{\partial x_j} = \alpha \frac{\omega}{k} \tau_{ij} \frac{\partial U_i}{\partial x_j} - \beta \omega^2 + \frac{\partial}{\partial x_j}\left[(\nu + \sigma \nu_t) \frac{\partial \omega}{\partial x_j} \right] \tag{5}$$

where τ_{ij} is the stress tensor, ν_t is the kinematic turbulent viscosity, and α, β, β^*, σ, and σ^* are the model closure coefficients.

The kinematic turbulent viscosity is evaluated as follows:

$$\nu_t = \frac{k}{\omega} \tag{6}$$

It was found that the k-ω model is the most suitable to predict Taylor–Couette flow among the other RANS models [26]. All the simulations are time-dependent, where the time step in degrees is fixed at $\Delta t = 90°$ reactor rotation and thus the equivalent time step in seconds will vary depending on the rotation speed (e.g., $\Delta t = 0.15$ s at 100 rpm and $\Delta t = 3.75 \times 10^{-3}$ s at 4000 rpm). The total time of each simulation varies from 120 s to 240 s depending on the flow conditions. Moreover, a steady solution is always reached before the end of the total simulation time.

3.2. Validation

The numerical approach discussed in the previous section needs to be validated against the experiment to make sure that it is suitable for Taylor–Couette flow. The experimental work by Wang et al. [27] was used for the validation and it consists of PIV measurements of the velocity field in a meridional plane of a turbulent Taylor–Couette flow reactor. The reactor has the following dimensions. The inner radius is R_i = 34.9 mm, the outer radius is R_o = 47.6 mm, and the length is L = 432 mm. The working fluid density is $\rho = 1720\ \mathrm{kg/m^3}$, the critical Taylor number is Ta_{cr} = 84.5, and the Taylor number ratio R = 34. Figure 4 compares the experimental and numerical velocity profiles of the flow with the annular gap at a radial distance r = 39.4 mm (one third of the annular gap starting from the inner cylinder). The numerical results show good agreement with the experimental measurements and can capture the vortical structure of the flow. In general, the k-ω model predicts both the mean axial and mean radial velocity fields reasonably well.

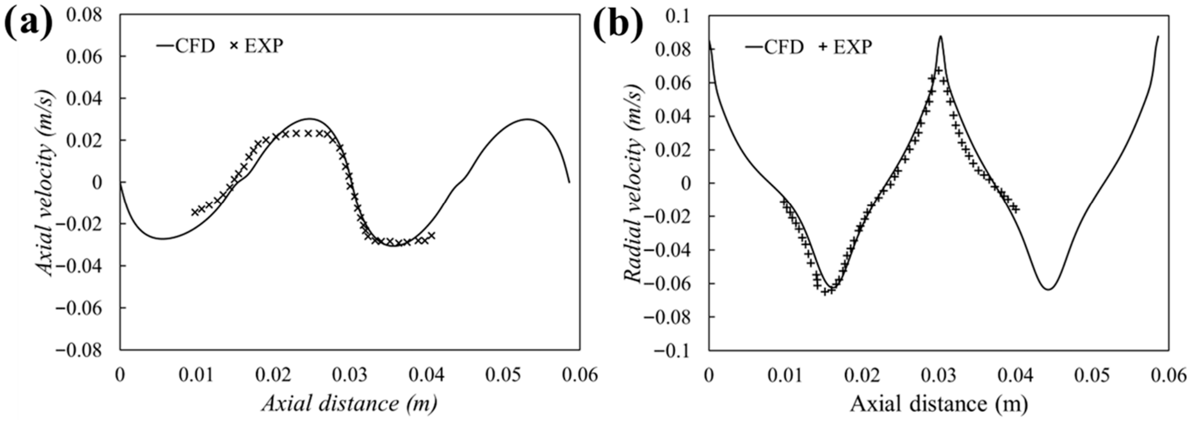

Figure 4. Comparisons of the experimental [27] and CFD velocity field (**a**) axial and (**b**) radial velocity profiles at r = 39.4 mm.

3.3. Numerical Geometry, Operating and Boundary Conditions

Figure 5 shows a 3D design of the reactor used in the simulations. Only a fraction of the central duct length is considered to reduce the computational cost. Thus, the numerical reactor is composed of an inner cylinder, inner duct, outer cylinder, and a plenum. This geometry is modelled using both two-dimensional (2D) axisymmetric and threedimensional (3D) approaches. Results from the 2D and 3D simulations will be compared later to show that the 2D approach is able to predict the mixing of Taylor–Couette flow with similar accuracy to the 3D approach. The gap size of the shown numerical geometry is d = 1 mm, and the radius ratio is η = 0.909, which suggests a first critical Taylor number (transition from Couette to Taylor flow) of Ta_{cr} = 139 according to the power law function in Figure 2. The transition to the turbulent Taylor flow regime occurs when the ratio of the current Taylor number to the critical Taylor number $(Ta/Ta_{cr}) = R \geq 20$, according to Di Prima and Swinney [2]. The effect of the gap size will be assessed later in the present work, and thus the radius ratio will change along with the critical Taylor number of each regime.

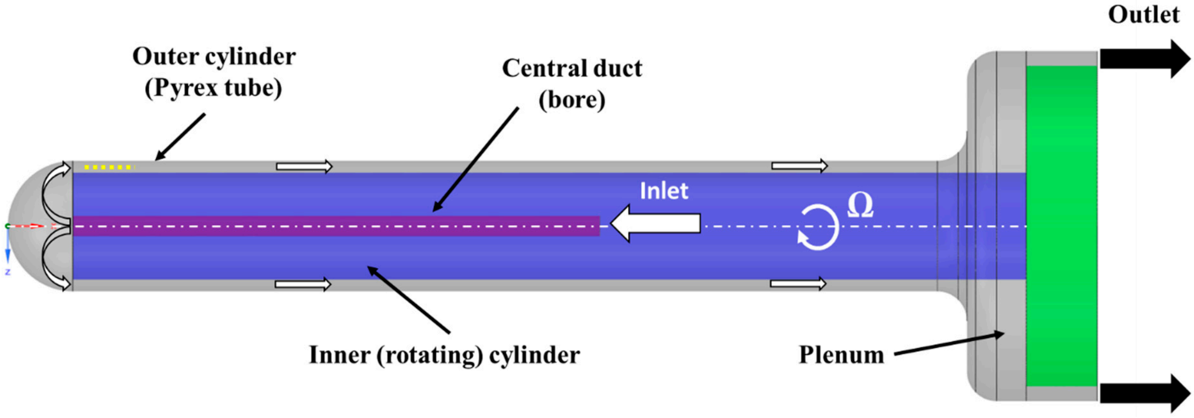

Figure 5. 3D design of the numerical geometry with the boundary conditions.

The reactor operates under atmospheric conditions (pressure P = 101,325 Pa and temperature T = 293 K). The working fluid is an organic chemical solution that has a density ρ = 959 kg/m^3 and a dynamic viscosity μ = 0.00069 kg/ms. The boundary conditions are imposed as follows. At the inlet of the central duct, a flow rate is imposed with a species mass fraction of the reactant Y_r = 1, a hydraulic diameter D_h = 3.4 mm, and a turbulence intensity I_t = 0.1%. Note that the hydraulic diameter and turbulence intensity are only specified for turbulent Taylor flow simulations as required by the turbulence model. At the outlet of the reactor, a static pressure is applied. A non-slip condition is imposed on all stationary and rotating walls. A rotation speed is applied on the inner cylinder about the X-axis. Moreover, this study will mainly focus on the laminar Taylor flow and turbulent Taylor flow regimes. The wavy and random regimes are not considered. The laminar regime is important because it initiates the formation of Taylor vortices, whereas the turbulent regime is more important because it generates the highest chemical yields, as reported in [21–24]. Therefore, the applied rotation speed will be adjusted to fit only these two regimes.

The organic photochemical reaction is not modelled in the present work. To the authors' knowledge, there are no CFD reaction models available in the literature that can describe organic photo-reactions. These types of reactions are very complex due to many aspects, such as the complexity of the organic molecules and compounds, the multichromatic nature of the light source used as it emits several wavelengths, the sensitivity of the compound absorbance to each wavelength, and the variation in the irradiance across the reactor surface and reagent. Thus, the reaction at the outer cylinder surface is simplified by imposing a constant mass fraction of the product Y_p to represent the formation of an organic compound at a constant reaction rate due to the photo-reaction. The dispersion of the organic product which is considered as a passive scalar (a passive tracer) is solved using the species transport formulation (Equation (3)). Both the reactant and the product have the same physical properties. At the beginning of the simulation, the flow is modelled without the species transport until the Taylor vortices are fully developed. Thereafter, the species transport is activated so that the product injected from the outer cylinder can be transported by the fully developed vortices. This numerical process replicates the experimental protocol [21], where the reactor is put on rotation to ensure the full formation of Taylor vortices, and then the light source is turned on to let the reaction take place.

This study will investigate the effect of four design parameters on the mixing efficiency of the reactor. The parameters are the annular gap size (d), the rotation speed of the inner cylinder (Ω), the flow rate ($\dot{V}$), and the fluid viscosity (μ). The values of these different parameters are summarised in Table 1 below.

Table 1. Summary of the investigated parameters.

Case	Ω (rpm)	d (mm)	η	Ta_{cr}	R	Regime	$\dot{V}$ (mL/min)	μ (kg/ms)	ρ (kg/m^3)
Gap size study	100	1	0.909	139	1.05	Laminar	2	0.00069	959
		2	0.818	99	2.65				
		3	0.727	83	4.21				
	2500	1	0.909	139	26.37	Turbulent	2	0.00069	959
		2	0.818	99	66.16				
		3	0.727	83	105.21				
Rotation speed study	2000	2	0.818	99	21.09	Turbulent	2	0.00069	959
	2500				26.37				
	3000				31.64				
	3500				36.91				
	4000				42.19				
Flow rate study	100	2	0.818	99	2.65	Laminar	5	0.00069	959
							10		
							15		
							20		
	2500				66.16	Turbulent	5	0.00069	959
							10		
							15		
							20		
Viscosity study	140	2	0.818	99	3.7	Laminar	2	0.00069	959
					2.88			0.00092	994
					1.19			0.00253	1125
	2500				66.16	Turbulent	2	0.00069	959
					51.43			0.00092	994
					21.17			0.00253	1125

3.4. Mesh Sensitivity Analysis

A mesh sensitivity analysis was conducted to assess the effect of the mesh density on the solution. Four meshes were generated for the 2D axisymmetric reactor geometry, which are coarse, medium, fine, and very fine, and they contain 82,543; 126,508; 158,938; and 185,138 cells, respectively. The main difference between these meshes is the number of nodes within the annular gap and through the annulus length, which is increased gradually from the coarse mesh to the very fine mesh. The four meshes are structured with a near wall distance $y^+ < 1$. A 3D mesh (Figure 6) was also generated to examine the effect of both the 2D and 3D approaches on the modelling of the Taylor–Couette flow. It is a hybrid mesh composed of hexahedral and polyhedral cells and it contains 4.5 million cells with $y^+ < 1$ and 42 cells with the gap.

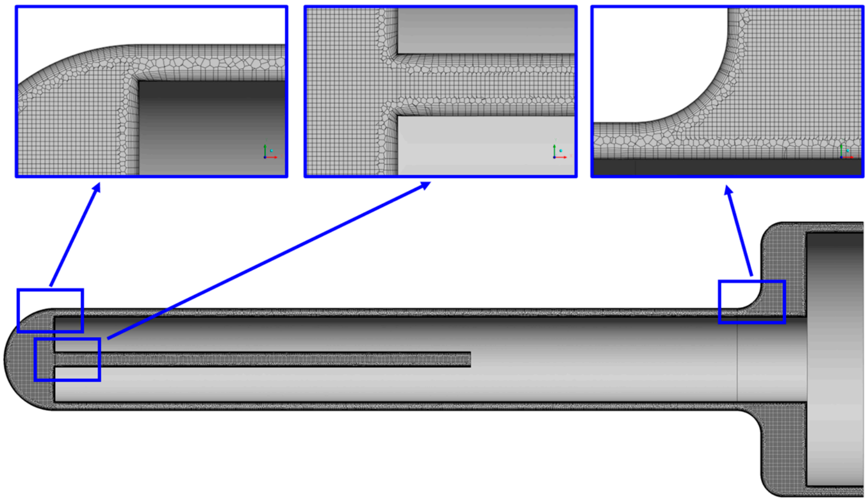

Figure 6. Cross section through the 3D reactor geometry showing the hybrid mesh used.

Figure 7 shows the velocity profiles at the centreline of the annular gap near the annulus inlet (see the yellow dashed line in Figure 5) predicted by the different 2D meshes at the flow rate $\dot{V}$ = 2 mL/min and Ω = 2500 rpm. The axial velocity profiles in Figure 7a indicate that the fine and very fine meshes provide similar results by predicting almost the same velocity peak and bottom. The coarse and medium meshes predict shifted profiles with the velocity peak and bottom of lower values indicating that the vortices are weaker, with a shifted position compared to the vortices of the fine and very fine meshes. For example, the axial velocity peaks are 0.034 m/s, 0.024 m/s, 0.041 m/s, and 0.039 m/s and are located at 0.0174 m, 0.0169 m, 0.0167 m, and 0.0167 m for the coarse, medium, fine, and very fine meshes, respectively. The radial velocity profiles in Figure 7b confirm that the fine and very fine meshes predict the same velocity values and vortex location compared to the coarse and medium meshes that show different results. Consequently, the coarse and medium meshes are not suitable for this study.

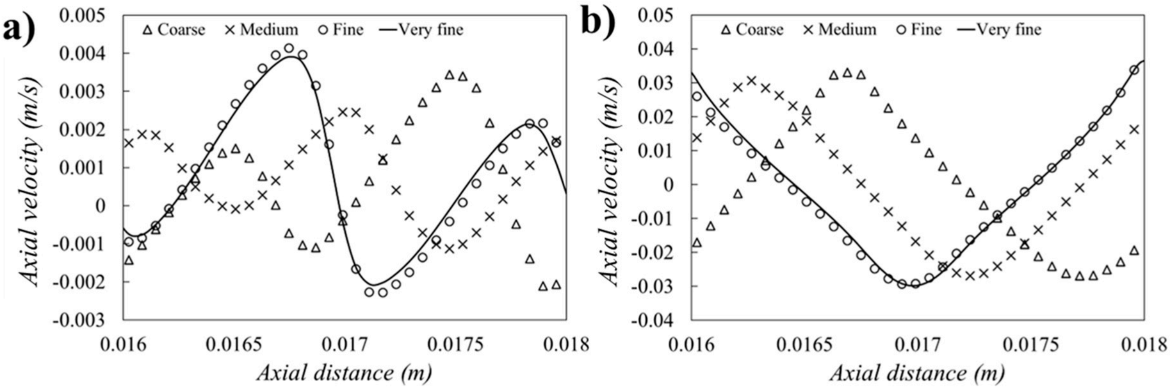

Figure 7. (**a**) Axial velocity profiles and (**b**) radial velocity profiles at the centreline of the annular gap for the different 2D meshes.

The effect of the mesh density on the mixing efficiency of the reactants was also analysed and is given in Figure 8. The mixing efficiency is an important indicator to inform the design of highly productive photo-chemical reactors. The toroidal motion of the vortices continuously replaces the fluid layer of the product formed near the outer cylinder (that is exposed to the source light) by a new fluid layer of the reactant to allow the photo-reaction to take place again. The dispersion of the product is called mixing and its efficiency (M_{eff}) is calculated using Equation (7) below. The maximum value of M_{eff} is 100% and it indicates that the maximum mass fraction (or concentration) of the product is reached everywhere in the reactor (in the present case, everywhere in the annulus).

$$M_{eff} = \left(1 - \frac{Y_p - Y_{p,ave}}{Y_p}\right) \times 100 \tag{7}$$

where Y_p is the mass fraction of the generated product at the outer cylinder and $Y_{p,ave}$ is the area-averaged value of the product's mass fraction through the whole annulus.

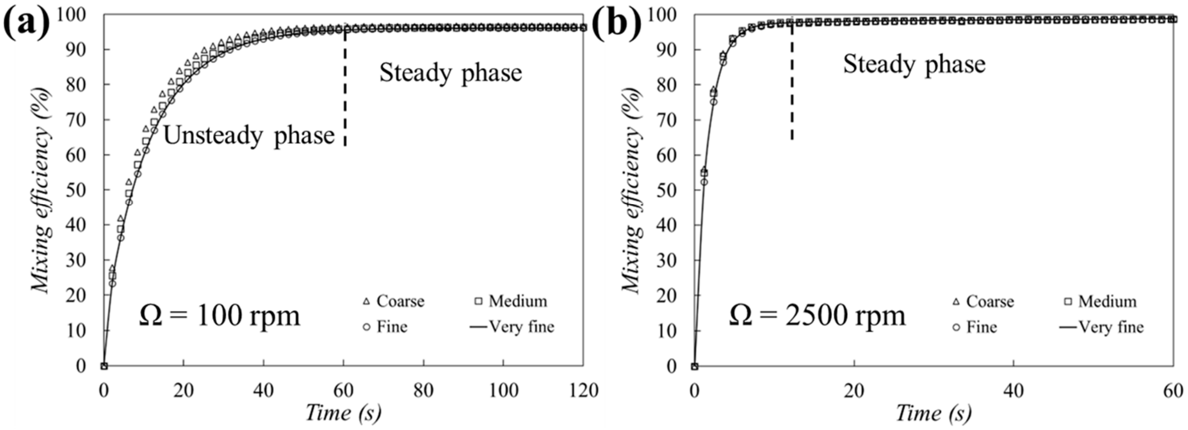

Figure 8. Time-dependent mixing efficiency for the different 2D meshes at (**a**) laminar regime at Ω = 100 rpm and (**b**) turbulent regime at Ω = 2500 rpm.

Results indicate that the mixing efficiency shows very low dependency on the mesh under the turbulent regime (e.g., Ω = 2500 rpm) and is more sensitive to the mesh under the laminar regime (e.g., Ω = 100 rpm), and this is only during the unsteady phase (e.g., $t < 60$ s), where the mixing efficiency keeps increasing to reach its maximum value after 60 s of reactor operation. For example, at $t = 21$ s, the mixing efficiency takes the values 86.31%, 83.45%, 81.52% and 81.47% for the coarse, medium, fine, and very fine meshes, respectively. This shows that the fine and very fine meshes predict almost the same mixing efficiency. From the results of the velocity profiles (Figure 7) and mixing efficiency (Figure 8), it can be concluded that the flow solution is independent of the fine and very fine meshes. Consequently, the fine mesh is adopted for the rest of the simulations shown in this study.

The effect of the modelling dimensions (2D or 3D) on the results was also examined. Figure 9 shows the evolution of the mixing efficiency predicted by the 2D and 3D modelling approaches at the flow rate $\dot{V} = 5$ mL/min. Both results show a good agreement and can capture almost the same evolution of the mixing efficiency under unsteady and steady phases. For example, the absolute difference in the mixing efficiency between 2D and 3D is 3% at $t = 40$ s and 1% at $t = 160$ s. In general, the 2D approach is used in the rest of the study since it predicts the increase in the mixing efficiency and its maximum value reasonably well.

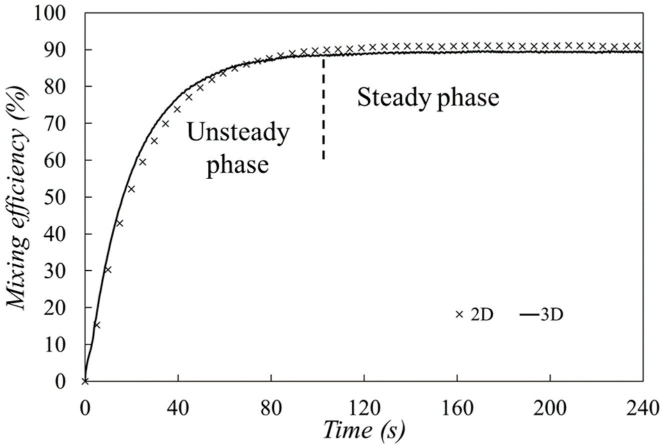

Figure 9. Time-dependent mixing efficiency for the 2D and 3D modelling approaches at Ω = 100 rpm.

It is important to note that M_{eff} is only time-dependent during the reaction start-up, and, once the photochemical conversion reaches a steady state, the mixing efficiency becomes constant. Thus, it is a measure of evaluating the reaction start-up performance. Until steadiness is reached, the solution exiting the reactor is actually a mixture of the original and produced compounds. This mixture can be easily reinjected to the reactor once the production reaches a steady state at near 100% mixing efficiency. Consequently, there will be no material waste, although the start-up mixture is only produced for 60 s for the laminar case and 14 s for the turbulent case.

4. Results and Discussion

4.1. Flow Field Within the Annulus Gap and Unsteady Product Transport

From the results of the previous section, one can note that the M_{eff} does not reach 100%, and even the best value reached is 98.9% for d = 1 mm at Ω = 2500 rpm (Figure 8b). This is due to the lack of mixing at the annulus inlet where the axial flow coming from the central duct starts interacting with the Taylor vortices. Figure 10 shows the distribution of the product mass fraction (Y_p) along with the flow field within the annular gap visualised using 2D streamlines. The flow exhibits two main features: the first one is the counter-rotating vortex pairs (white streamlines), and the second one is the winding flow (black streamlines). The winding flow is formed due to the penetration of the axial flow between the vortices, which makes the fluid flow up and down alternately around the vortices. A similar flow structure was experimentally found by Wereley and Lueptow [28]. The vortices located towards the inner cylinder are rotating in the clockwise direction and they are slightly larger than those towards the outer cylinder, which rotate in the anti-clockwise direction. It appears that the winding flow initially flows between the outer cylinder and the first clockwise vortex and transports the generated product away from the outer cylinder. At this location (the annulus inlet), the product concentration is the lowest compared to the rest of the annular gap, which explains why the M_{eff} cannot reach 100%. Moreover, the anti-clockwise vortices (AVs) promote more mixing since they are in direct contact with the generated product at the outer cylinder, whereas the clockwise vortices (CVs) contribute less to the mixing because of the winding flow that prevents their contact with the outer cylinder.

Figure 11 shows the unsteady transport of the product visualised using snapshots of the product mass fraction contours near the mid region of the annulus (L > 100 mm). The Taylor vortices can be easily seen and even the CV and AV cells can be easily distinguished at the first few instants (e.g., t = 1.95 s and t = 2.85 s), where the AV cells contain low product concentration ($Y_p < 0.03$) and the CV cells almost contain only reactant ($Y_r \approx 0.1$). The early

AV cells contain the product because of their direct contact with the outer cylinder. The early CV cells do not contain the product because of the winding flow that separates them from the outer cylinder. It can also be seen that the vortices are moving (see the plus mark) due to the winding flow that transports them axially. The axial speed of the vortices is at 0.076 mm/s, whereas the axial flow imposed at the inner duct inlet is 0.5 mm/s. This shows that the vortices speed (known as vortex drift) is about 6.5 times slower than the axial flow. Both the vortices rotation and axial displacement contribute to the mixing, and the product dispersion is increasing gradually during the unsteady phase of the flow. It appears that the axial winding flow has a significant advantage, which consists in carrying out a continuous reaction process by transporting the vortices. However, it has the drawback of causing the vortex pairs to promote mixing at different paces.

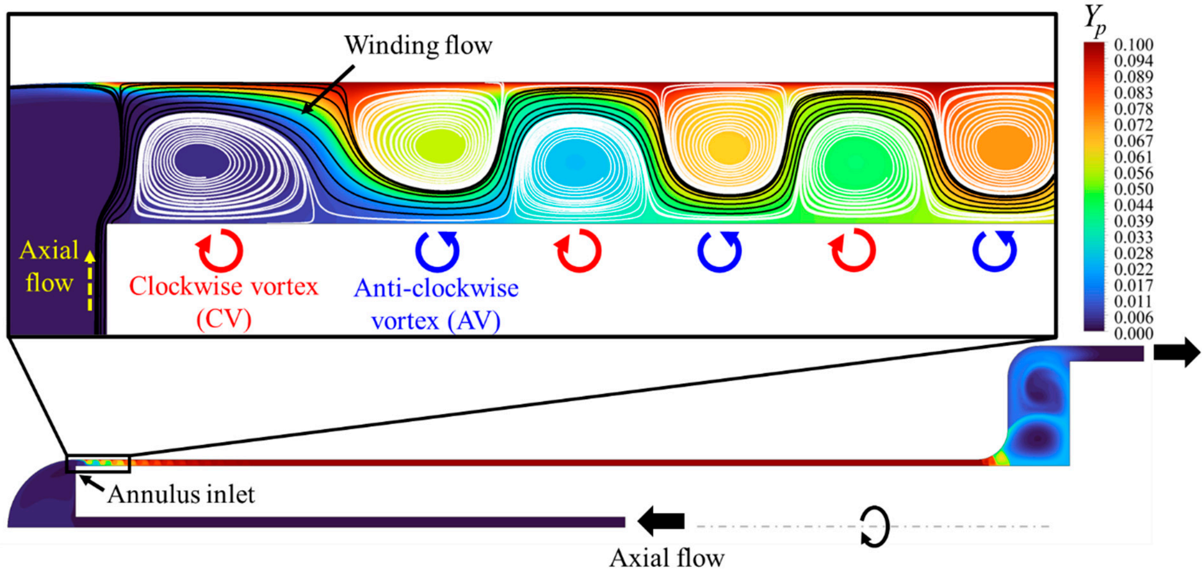

Figure 10. Flow structure and product mass fraction distribution near the annulus inlet ($d = 1$ mm, $\Omega = 100$ rpm, and $\dot{V} = 2$ mL/min).

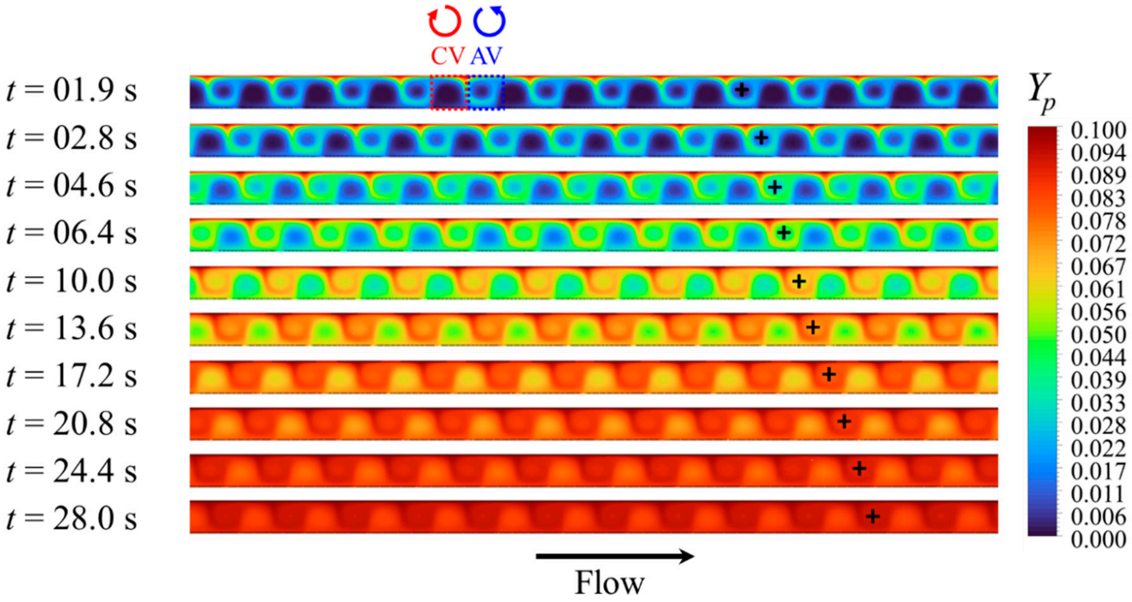

Figure 11. Unsteady contours of the product mass fraction near the mid annulus region ($d = 1$ mm, $\Omega = 100$ rpm, and $\dot{V} = 2$ mL/min).

4.2. Effect of the Gap Size on the Mixing Efficiency

Three reactors with three different gap sizes, d = 1 mm, 2 mm, and 3 mm, are designed and evaluated, and they have the radius ratios η = 0.909, 0.818, and 0.727, respectively. The diameter of the inner rotating cylinder is reduced to change the gap width while the diameter of the outer cylinder is kept constant. The change in the mixing efficiency within the annular gap is monitored under both the laminar and turbulent regimes for all the gap sizes at $\dot{V}$ = 2 mL/min. Note that increasing the gap size at a constant flow rate will reduce the average axial flow velocity within the annulus. Thus, a delay in reaching the maximum efficiency is expected for larger gap size cases. The results are plotted in Figure 12. It was previously shown (Section 3.4) that the evolution of the M_{eff} can be divided into two phases, where the first phase is unsteady and shows the increase in the M_{eff} until it reaches its maximum amount, and the second phase is steady and shows a constant mixing efficiency. The unsteady phase represents the formation of the product and its dispersion within the annular gap of the reactor. The point where the M_{eff} reaches the maximum value indicates the steady phase onset and defines the equilibration time that shows whether the mixing is slow or fast. In general, and for both regimes, it appears that the equilibration time is very sensitive to the gap size. However, the maximum M_{eff} is only slightly sensitive to the gap size. Under the laminar regime (e.g., Ω = 100 rpm), the equilibration time is higher for the large gap size of d = 3 mm, as expected, and this is due to the increase in the residence time within the reactor. The increase in the gap size leads to an increase in the reactor volume, and consequently the residence time increases at a constant flow rate. The equilibration time is 64 s, 104 s, and 222 s for d = 1 mm, 2 mm, and 3 mm, respectively, showing a more delayed equilibration for larger gaps, as expected. Thus, the equilibration time is delayed by 38.5% and 71.2% for d = 2 mm and 3 mm, with regard to the equilibration time of d = 1 mm. The effect of the gap size change on the maximum M_{eff} reached is almost negligible, which is around 96% for all the configurations. Under the turbulent regime (e.g., Ω = 2500 rpm), the mixing is expected to enhance as the shear force of the vortices increases, which improves (reduces) the equilibration time. The steady phase onset is drastically reduced to reach 21.6 s, 38.4 s, and 84 s for d = 1 mm, 2 mm, and 3 mm, respectively. This provides an equilibration time reduction of 66.2%, 63.0%, and 62.1%, with regard to the laminar case from the smallest to the largest gap widths, respectively. The effect of the gap size change on the maximum M_{eff} at this high rotation speed is small, where M_{eff} = 98.9%, 97.8%, and 96.3% for d = 1 mm, 2 mm, and 3 mm, respectively. It can be said that the increase in the gap size does not appear to improve or worsen the mixing efficiency. However, it delays the equilibration time, meaning that it slows down the mixing process. Another contributor to delaying the equilibration time could be the winding flow, as it should be altered when the gap size changes, as will be revealed in Section 4.3.

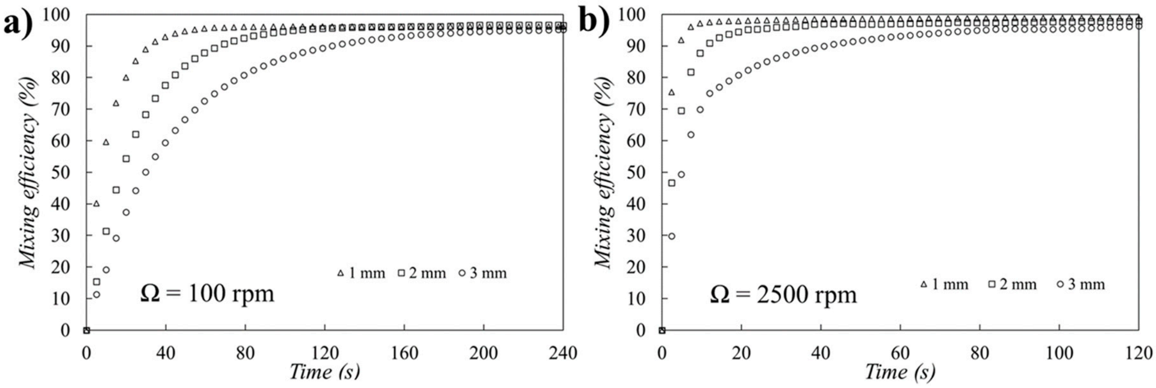

Figure 12. Time-dependent mixing efficiency for the different gap sizes (d = 1, 2, 3 mm) at $\dot{V}$ = 2 mL/min and under (**a**) laminar Taylor regime at Ω = 100 rpm and (**b**) turbulent Taylor regime at Ω = 2500 rpm.

4.3. Effect of the Gap Width on the Flow Structure and Product Distribution

Figure 13a shows the instantaneous flow field and product contours for the three investigated gap sizes at t = 1.95 s under laminar flow condition. The vortices are indicated using white streamlines and the winding flow is indicated using red streamlines. Figure 13b schematises the flow structure within the annular gap and shows the interaction between the vortices and the winding flow. One can see that the increase in the gap width leads to an increase in the size of the vortices, as expected. The length of the vortex pairs (both the CV and AV known as wavelength) is L_v = 2 mm, 3.5 mm, and 4.4 mm for d = 1 mm, 2 mm, and 3 mm, respectively. In addition, the increase in the gap width reduces the width of the winding flow. It seems that larger vortices tend to contract the winding flow to occupy more space within the annular gap. An experiment from Koschmieder [29] shows that the wavelength under the laminar Tylor regime without winding flow is approximately two times the gap width, such as $L_v \approx 2$ d for a gap radius ratios η = 0.896. Comparison with the present simulation confirms that Koschmieder's [29] finding is true for the gap width case of d = 1 mm, which corresponds to η = 0.909, which is very close to the experimental η = 0.896. However, when the gap width increases, this rule becomes invalid and the wavelength becomes smaller than two times the gap width. It takes the value of L_v = 1.75 d and 1.46 d for d = 2 mm and 3 mm, respectively. Moreover, the increase in the vortices size is accompanied with a decrease in the product concentration, particularly within the AV cell. The area-average value of the product mass fraction of the AV cell is 0.0077, 0.0053, and 0.0036 for d = 1 mm, 2 mm, and 3 mm, respectively. Larger vortices require more time to transport the product, which explains the slower mixing process and higher equilibration time found in the larger gap size cases, as reported in Figure 12. In other words, larger vortices impose a larger vertical distance towards the inner tube that the winding flow must travel, hence contributing to the delayed equilibration time (higher residence time) at larger gap sizes, as reported in Figure 12.

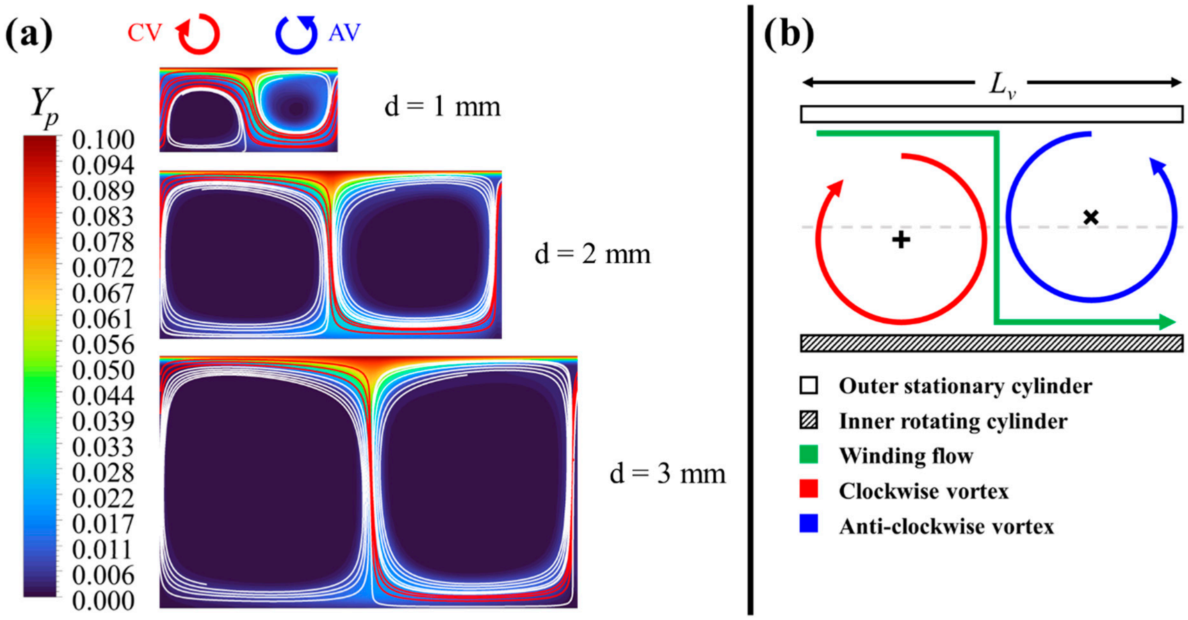

Figure 13. (**a**) Flow structure and product distribution of a vortex pair for the different gap sizes at t = 1.95 s and Ω = 100 rpm. (**b**) A schematic drawing of the flow structure of Taylor–Couette flow coupled with an axial flow. The plus and cross signes show the vortices centres.

4.4. Effect of the Rotational Speed on the Mixing Efficiency

Studying the effect of the rotational speed on the mixing efficiency is of great importance because it helps identify the optimal operational speed. Previous experiments by

Lee et al. [22] of this reactor configuration showed that the conversion of a given chemical compound reaches the highest values (almost 100%) at high rotation speeds corresponding to the turbulent Taylor regime ($\Omega \geq 3000$ rpm for the given chemical compound), whereas, under the laminar Taylor ($\Omega = 500$ rpm) and Taylor wavy ($\Omega = 1500$ rpm) regimes, the conversion is lower, and reached 55% and 70%, respectively. Thus, this sub-section intends to focus on the effect of the rotation speed on the mixing efficiency under the turbulent regime only. The gap size used for this investigation is $d = 2$ mm. The transition onset to the turbulent Taylor regime is at $\Omega = 2000$ rpm, which corresponds to the Taylor number ratio $R = 21.09$. Five rotation speeds are tested: $\Omega = 2000$; 2500; 3000; 3500; 4000 rpm. The evolution of the M_{eff} under the different rotation speeds is plotted in Figure 14. The results show that the M_{eff} increases as the rotation speed increases too, and this is during the unsteady phase only. For example, at $t = 5$ s, $M_{eff} = 65.7\%$, 69.5%, 72.9%, 75.2%, and 77.0% for the lowest to the highest rotation speeds, respectively. When the steady phase is reached, the mixing efficiency takes the same value of 98% for all the rotation speeds. This finding is in accordance with the experimental observations by Lee et al. [22], where they reported a constant chemical conversion at turbulent rotations speeds. Moreover, the optimal operational speed is $\Omega = 2000$ rpm and higher values will lead to consuming more electric energy by the driving motor without improving the mixing efficiency.

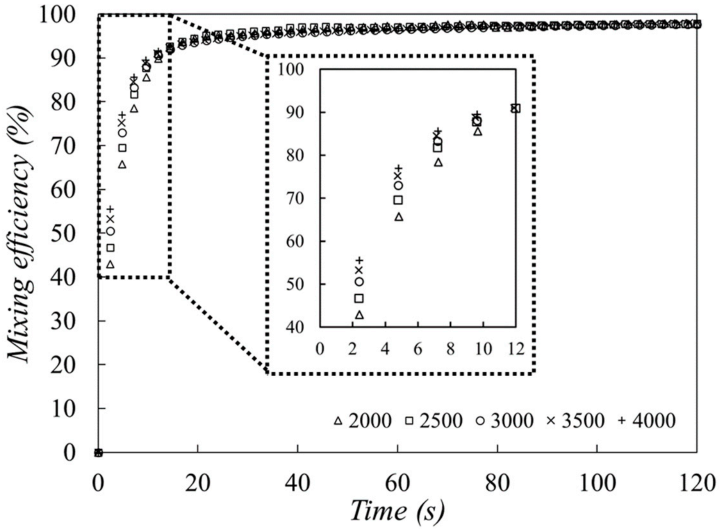

Figure 14. Time-dependent mixing efficiency for the different turbulent rotation speeds at $d = 2$ mm.

4.5. Effect of the Flow Rate on the Mixing Efficiency

The increase in the flow rate aiming to increase the productivity of chemical compounds is always desirable. However, it was found that the increase in the flow rate leads to a decrease in the yield [22], and this could be attributed to the deterioration of the mixing process and decrease in residence time. This sub-section focuses of the effect of the flow rate of the mixing efficiency under the laminar Taylor ($\Omega = 100$ rpm) and turbulent ($\Omega = 2000$ rpm) regimes. Four flow rates are investigated, which are $\dot{V} = 5$; 10; 15; and 20 mL/min. Figure 15a shows the temporal evolution of the mixing efficiency for the different flow rates under laminar Taylor flow. The increase in the flow rate affects both the equilibration time and maximum mixing efficiency. The equilibration time takes the values $t = 123.7$ s 113.9 s 94.0 s, and 74.2 s for $\dot{V} = 5$ mL/min, 10 mL/min, 15 mL/min, and 20 mL/min, respectively, whereas the maximum M_{eff} reached is 90.6%, 80.1%, 68.0%, and 57.4% for the lowest to the highest flow rates, respectively. These findings suggest that the higher the flow rate, the faster the equilibration time and the lower the mixing efficiency. It seems that the increase in the flow rate strengthens the winding flow that reduces the size of the vortices, and consequently the mixing process deteriorates, as will be explained later. Moreover, Figure 15b shows the temporal evolution of the mixing efficiency for the different flow rates under turbulent regime. The operation of the reactor under high rotation speed brings a significant improvement in both the equilibration time and maximum M_{eff}. The equilibration time takes the values t = 36 s, 31.2 s, 24 s, and 16.8 s and the maximum M_{eff} reached is 95.8%, 93.4%, 91.0%, and 88.4% for $\dot{V}$ = 5 mL/min, 10 mL/min, 15 mL/min, and 20 mL/min, respectively. Comparing with the laminar Taylor flow at the highest flow rate ($\dot{V}$ = 20 mL/min), the reactor gained 75.5 s in equilibration time and 31.1% of mixing efficiency by operating under the turbulent regime. This gain is due to the transfer of higher momentum from the rotating cylinder to the vortices that exhibit higher toroidal motion with highly efficient radial mixing.

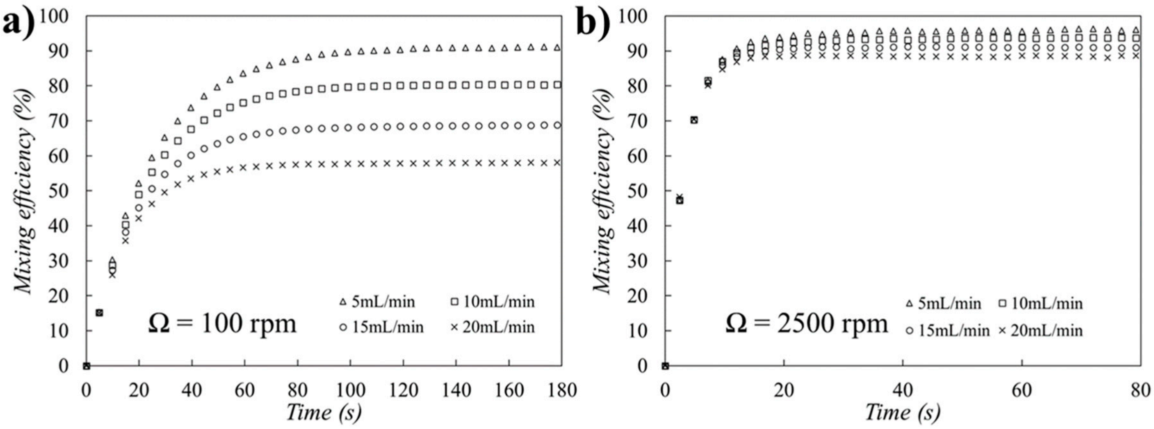

Figure 15. Time-dependent mixing efficiency for the different flow rates under (**a**) laminar Taylor regime at Ω = 100 rpm and (**b**) turbulent Taylor regime at Ω = 2500 rpm.

4.6. Effect of the Flow Rate on the Flow Structure and Product Distribution

Figure 16a,b show the instantaneous (t = 17.2 s) flow structure and product contours at a length equivalent to one vortex pair, for the different flow rates examined under the laminar Taylor regime. The flow structure is visualised using 2D streamlines, where the red streamlines represent the winding flow, and the black streamlines show the vortices. When the flow rate increases, the winding stream dominates the flow field with an increased width (λ), which contracts the Taylor vortices. The winding stream widths are λ = 0.23 mm, 0.36 mm, 0.517 mm, and 0.674 mm for $\dot{V}$ = 5 mL/min, 10 mL/min, 15 mL/min, and 20 mL/min, respectively. A blockage ratio B_r can be defined as the ratio of λ to the gap width (d = 2 mm), which equates to B_r = 11.5%, 18%, 25.85%, and 33.7% for the lowest to the highest flow rates, respectively. The higher the blockage ratio, the lower the vortices size, and consequently the weaker the vortices are. The length of a vortex pair including the winding stream is L_v = 2.1 mm, 1.9 mm, 1.3 mm, and 1.1 mm for the lowest to the highest flow rates, respectively. When L_v is reduced, the core of the vortices (see the blue line linking the AV and CV centres) are no longer aligned with the annular gap centreline, and they tend to be inclined, which is a sign of vortex weakness. The inclination is quantified by the angle β = 2.9°, 5.4°, 11.9°, and 19.9° for $\dot{V}$ = 5 mL/min, 10 mL/min, 15 mL/min, and 20 mL/min, respectively. The continuous increase in the flow rate deteriorates the dispersion and transport of the product, as indicated in Figure 16b. On the one hand, the wide winding stream isolates more and more of the CV from the outer cylinder where the product is generated; as a result, the CV cell ends up with almost zero product within its core at $\dot{V}$ = 20 mL/min. On the other hand, the weakening effect of the vortices is clearly visible for the AV cell, where it contains less and less product, even though it is always in direct contact with the outer cylinder. Consequently, both the AV cell weakening and

CV cell isolation contribute to the decrease in the mixing efficiency found in Figure 15a at the laminar Taylor regime (Ω = 100 rpm). Radial profiles of the product mass fraction are plotted through the CV cell (red dashed line) in Figure 17 to quantify the loss of the product within this vortex. It can be seen that the product quantity is drastically decreased when the flow rate goes from 5 to 20 mL/min. The winding stream region (d > 10.32 mm) has the highest product concentration, whereas the mid gap region ($d \approx 10$ mm) suffers from low product concentration. At the rotating cylinder (d = 9 mm), the product mass fraction is Y_p = 0.0736, 0.0386, 0.017, and 0.0057 for $\dot{V}$ = 5 mL/min, 10 mL/min, 15 mL/min, and 20 mL/min, respectively. The average values of the profiles are 0.0708, 0.0369, 0.0208, and 0.0145 for the lowest to the highest flow rate. The results indicate that only 70.8% of the product is transported through the CV cell at the lowest flow rate (5 mL/min) and 14.5% is transported at the highest flow rate (20 mL/min), which is a 56.3% decline in the mixing efficiency.

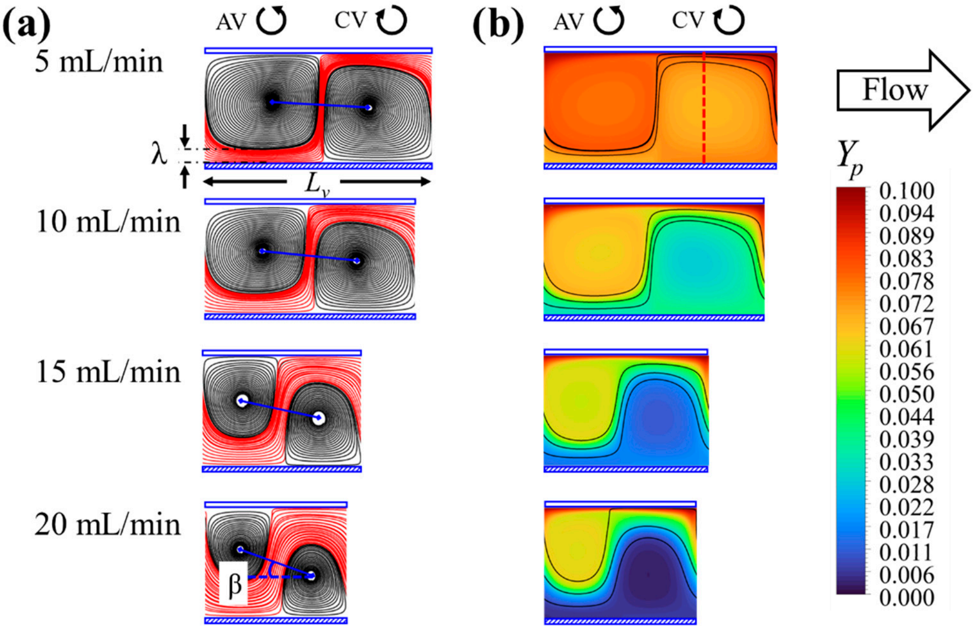

Figure 16. Instantaneous (**a**) flow structure and (**b**) product contours at laminar regime Ω = 100 rpm for the different investigated flow rates.

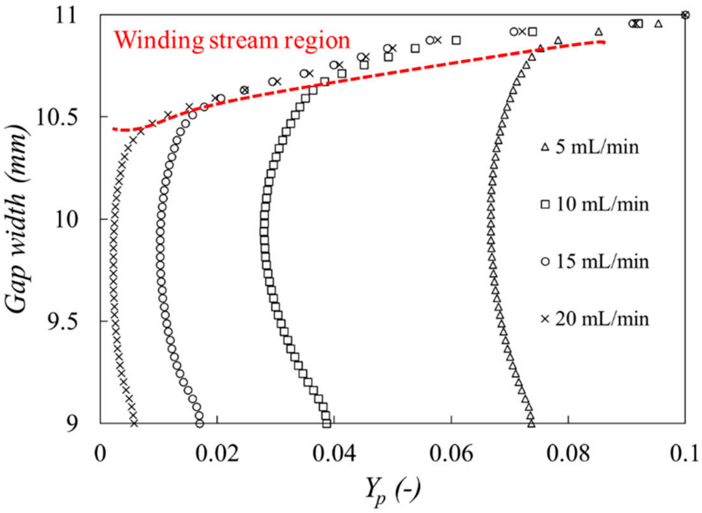

Figure 17. Radial profiles of the product mass fraction through the CV cell for the different investigated flow rates.

Figure 18a,b show the instantaneous (t = 17.25 s) flow structure and product contours at a length equivalent to one vortex pair and $\dot{V}$ = 20 mL/min under the turbulent Taylor regime. One can note that the turbulent flow behaviour is significantly different when compared to the laminar flow behaviour (Figure 16a) at this same flow rate. Two small new vortices (see red streamlines) are formed near the outer cylinder at the inflow direction and are in contact with the Taylor vortex pairs. The first small vortex is rotating in the clockwise direction, which is in contact with the AV and is called (SCWV). The second small vortex is rotating on the anti-clockwise direction, which is in contact with the CV and is called (SAWV). Moreover, the turbulent vortex pairs feature a larger size (L_v = 2.52 mm), which is 55.2% larger than the length of the laminar vortex pairs. The average blockage ratio is B_r = 3% (λ = 0.06 mm), which is almost 90% smaller than B_r of the laminar vortex pairs. Indeed, longer vortices with smaller winding stream width will significantly enhance the mixing and transport of the product, as reflected in Figure 18b, where high product concentration dominates the flow field. It appears that the newly formed small vortices are also contributing to enhancing the mixing locally, as they feature the highest product concentration due to the direct contact with the outer wall.

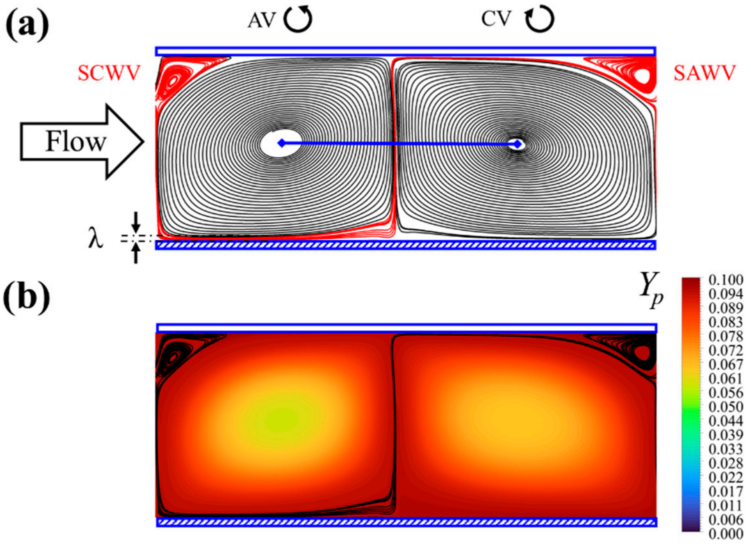

Figure 18. Instantaneous (**a**) flow structure and (**b**) product contours at $\dot{V}$ = 20 mL/min and under turbulent regime.

4.7. Effect of the Fluid Viscosity on the Mixing Efficiency

The effect of the working fluid viscosity is one of the key parameters that affects the design of the photo-vortex reactor, as the change in the viscosity directly alters the Taylor number and consequently the flow regime, and ultimately the mixing efficiency of the reactor. Early experiments of Taylor–Couette flows (not a reactor configuration) showed that the viscosity increase results in a decrease in the number of vortices present in the annular gap [2]. Very recent results from another variety of the present photo-vortex reactor, which is an electrochemical Taylor vortex reactor [24], showed that highly concentrated (more viscous) solutions lead to slower equilibration time. Thus, this sub-section focuses of the effect of the dynamic viscosity of the equilibration time and mixing efficiency under both laminar and turbulent regimes. Three different solutions with different dynamic viscosities (as shown in Table 1) are used: μ = 0.00069 kg/m·s, 0.00092 kg/m·s, 0.00253 kg/m·s, and are called Solultion-1, Solultion-2, and Solultion-3, respectively. Figure 19 shows the temporal evolution of the mixing efficiency for the different solutions. It can be seen that the increase in the viscosity does not affect the maximum mixing efficiency, but it only alters the equilibration time. At the laminar regime (Ω = 140 rpm), the equilibration time is the same for Solultion-1 and Solultion-2, which is t = 116.7 s; however, it is 26.6% higher for the more viscous fluid (Solution-3, t = 159.1 s). The Taylor number ratio at this low rotation speed is $Ta/Ta_{cr} = R$ = 3.7, 2.88, and 1.19 for the less viscous to the high viscous solutions. Lower Ta/Ta_{cr} indicate that annular gap vortices extract less momentum from the rotating cylinder, which leads to slow mixing. At the turbulent regime (Ω = 2500 rpm), the equilibration time reaches 26.4 s for both Solution-1 and Solution-2, which is 77% less than the equilibration time of the laminar case, for the same solutions. For the more viscous Solultion-3, it is 38.4 s, which is 75.8% less than the equilibration time of the laminar case of the same solution. The turbulent Taylor number ratio is 66.1, 51.4, and 21.2 for Solution-1, Solution-2, and Solution-3, respectively. It can be concluded that the operation of the photo-vortex reactor under the turbulent regime brings a significant improvement in the equilibration time. This is due to the higher rotational momentum transfer to the vortices that generate fast mixing of the solution and hence lower equilibration time is achieved.

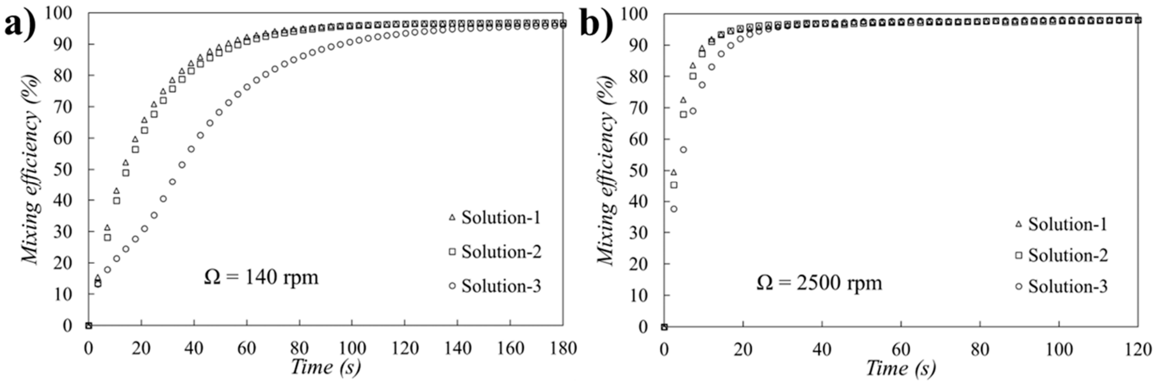

Figure 19. Time-dependent mixing efficiency for the different fluid viscosities, (**a**) laminar Taylor regime at Ω = 100 rpm and (**b**) turbulent Taylor regime at Ω = 2500 rpm.

5. Conclusions

In this work, the mixing efficiency and equilibration time of a novel photochemical Taylor–Couette flow reactor were investigated. The reactor was a subject of numerical simulations that evaluated different design parameters affecting its performance. The flow structure and product concentration were visualised using streamlines and product contours. The flow was found to be complex and featured counter-rotating vortex pairs and a winding steam that flowed around the vortices. The vortex pairs were (1) an anti-clockwise vortex that promoted high mixing because of its direct contact with the reaction zone (the outer cylinder) and (2) a clockwise vortex that contributed less to mixing because it is separated from the reaction zone by the winding flow.

The temporal evolution mixing efficiency with the annuls was plotted for each of the investigated parameters and under both laminar and turbulent regimes. The results revealed that the mixing efficiency profile is composed of an unsteady phase representing the increase in the mixing due to the Taylor–Couette flow, and a steady phase is steady where a maximum mixing level is reached and maintained. The onset of the steady phase is called the equilibration time.

The parameters of gap width, rotation speed, and fluid viscosity were found to mainly affect the equilibration time and not the maximum mixing efficiency reached. The increase in the gap width led to an increase in the Taylor vortices size, which increased the residence time, and consequently the equilibration time increased too. The increase in the fluid's viscosity reduced the Taylor number, which meant that less momentum was transferred from the rotating cylinder to the fluid. However, flow rate was identified as the sole parameter that affected the mixing efficiency. The increase in the flow rate strengthened the winding flow and contracted the vortices, which reduced their contact with the reaction zone, and consequently the mixing deteriorated. Moreover, one solution to improve the mixing efficiency at high flow rates was to operate the reactor under the turbulent regime (high rotation speed), which led to an improvement of 31.1% compared to operating under a laminar regime (low rotation speed).

Author Contributions: Z.M.: Conceptualisation, methodology, software, validation, formal analysis, investigation, data curation, writing—original draft preparation, writing—review and editing, visualisation. R.J.-L.: Conceptualisation, methodology, resources, writing—original draft preparation, supervision, writing—review and editing, funding acquisition. S.J.P.: Conceptualisation, methodology, resources, supervision, writing—review and editing, project administration, funding acquisition. M.W.G.: Conceptualisation, methodology, project administration, resources, writing—review and editing, project administration, funding acquisition. All authors have read and agreed to the published version of the manuscript.

Funding: We thank the UKRI for the Programme Grant [EP/P013341/1] and the HPC Midlands+ [EP/T022108/1] Consortium for providing the High-Performance Computing Facility [Sulis].

Institutional Review Board Statement: Not applicable.

Informed Consent Statement: Not applicable.

Data Availability Statement: The original contributions presented in this study are included in the article.

Acknowledgments: The authors are grateful to Martyn Poliakoff, Richard Brown, Darren Lee, and Gabriele Gennari for helpful discussions.

Conflicts of Interest: The authors declare no conflicts of interest.

References

1. Taylor, G.I., VIII. Stability of a viscous liquid contained between two rotating cylinders. *Philos. Trans. R. Soc. Lond.* **1923**, *223*, 289–343. [CrossRef]
2. Prima, R.C.; Swinney, H.L. Instabilities and transition in flow between concentric rotating cylinders. In *Topics in Applied Physics*; Springer: Berlin/Heidelberg, Germany, 1981; pp. 139–180.
3. Simmers, D.A.; Coney, J.E.R. The experimental determination of velocity distribution in annular flow. *Int. J. Heat Fluid Flow* **1979**, *1*, 177–184. [CrossRef]
4. Heinrichs, R.M.; Cannell, D.S.; Ahlers, G.; Jefferson, M. Experimental test of the perturbation expansion for the Taylor instability at various wavenumbers. *Phys. Fluids* **1988**, *31*, 250–255. [CrossRef]
5. Takeda, Y.; Fischer, W.E.; Sakakibara, J. Decomposition of the modulated waves in a rotating couette system. *Science* **1994**, *263*, 502–505. [CrossRef]
6. Wereley, S.T.; Lueptow, R.M. Spatio-temporal character of non-wavy and wavy Taylor–Couette flow. *J. Fluid Mech.* **1998**, *364*, 59–80. [CrossRef]
7. Nemri, M.; Charton, S.; Climent, E. Mixing and axial dispersion in Taylor–Couette flows: The effect of the flow regime. *Chem. Eng. Sci.* **2016**, *139*, 109–124. [CrossRef]
8. Nemri, M.; Climent, E.; Charton, S.; Lanoë, J.Y.; Ode, D. Experimental and numerical investigation on mixing and axial dispersion in Taylor–Couette flow patterns. *Chem. Eng. Res. Des.* **2013**, *91*, 2346–2354. [CrossRef]
9. Wang, H. Experimental and Numerical Study of Taylor-Couette Flow. Doctoral Dissertation, Iowa State University, Ames, LA, USA, 2015. [CrossRef]
10. Hwang, J.Y.; Yang, K.S. Numerical study of Taylor–Couette flow with an axial flow. *Comput. Fluids* **2004**, *33*, 97–118. [CrossRef]
11. Gao, X.; Kong, B.; Dennis Vigil, R. CFD simulation of bubbly turbulent Tayor–Couette flow. *Chin. J. Chem. Eng.* **2016**, *24*, 719–727. [CrossRef]
12. Li, G.; Yang, X.; Ye, H. CFD simulation of shear flow and mixing in a Taylor–Couette reactor with variable cross-section inner cylinders. *Powder Technol.* **2015**, *280*, 53–66. [CrossRef]
13. Chung, S.Y.; Sung, H.J. Large-eddy simulation of turbulent flow in a concentric annulus with rotation of an inner cylinder. *Int. J. Heat Fluid Flow* **2005**, *26*, 191–203. [CrossRef]

14. Cheng, W.; Pullin, D.I.; Samtaney, R. Large-eddy simulation and modelling of Taylor–Couette flow. *J. Fluid Mech.* **2020**, *890*, A17. [CrossRef]
15. Dong, S. Direct numerical simulation of turbulent Taylor–Couette flow. *J. Fluid Mech.* **2007**, *587*, 373–393. [CrossRef]
16. Anabaraonye, B.U.; Bentzon, J.R.; Khaliqdad, I.; Feilberg, K.L.; Andersen, S.I.; Walther, J.H. The influence of turbulent transport in reactive processes: A combined numerical and experimental investigation in a Taylor-Couette reactor. *Chem. Eng. J.* **2021**, *421*, 129591. [CrossRef]
17. Qin, K.; Li, D.; Huang, C.; Sun, Y.; Wang, J.; Luo, K. Numerical investigation on heat transfer characteristics of Taylor Couette flows operating with CO_2. *Appl. Therm. Eng.* **2020**, *165*, 114570. [CrossRef]
18. Park, Y.G.; Kim, K.T. Selective separation of various heavy metals from synthesized phosphoric acid solutions. *J. Ind. Eng. Chem.* **2021**, *95*, 267–276. [CrossRef]
19. Yoon, S.H.; Lim, J.G.; Hong, J.; Han, S.-K.; Kim, M.K.; Choi, J.-B.; Lee, T.-R. Numerical simulation of ammonium perchlorate particles based on a population balance equation model in Taylor-Couette flow. *J. Ind. Eng. Chem.* **2020**, *89*, 280–287. [CrossRef]
20. Manikandan, N.A.; Pakshirajan, K.; Pugazhenthi, G. A novel rotating wide gap annular bioreactor (Taylor-Couette type flow) for polyhydroxybutyrate production by Ralstonia eutropha using carob pod extract. *J. Environ. Manag.* **2021**, *299*, 113591. [CrossRef]
21. Lee, D.S.; Sharabi, M.; Jefferson-Loveday, R.; Pickering, S.J.; Poliakoff, M.; George, M.W. Scalable continuous vortex reactor for gram to kilo scale for UV and visible photochemistry. *Org. Process Res. Dev.* **2020**, *24*, 201–206. [CrossRef]
22. Lee, D.S.; Amara, Z.; Clark, C.A.; Xu, Z.; Kakimpa, B.; Morvan, H.P.; Pickering, S.J.; Poliakoff, M.; George, M.W. Continuous photo-oxidation in a vortex reactor: Efficient operations using air drawn from the laboratory. *Org. Process Res. Dev.* **2017**, *21*, 1042–1050. [CrossRef]
23. Love, A.; Lee, D.S.; Gennari, G.; Jefferson-Loveday, R.; Pickering, S.J.; Poliakoff, M.; George, M. A continuous-flow electrochemical Taylor vortex reactor: A laboratory-scale high-throughput flow reactor with enhanced mixing for scalable electrosynthesis. *Org. Process Res. Dev.* **2021**, *25*, 1619–1627. [CrossRef]
24. Lee, D.S.; Love, A.; Mansouri, Z.; Clarke, T.H.W.; Harrowven, D.C.; Jefferson-Loveday, R.; Pickering, S.J.; Poliakoff, M.; George, M.W. High-productivity single-pass electrochemical Birch reduction of naphthalenes in a continuous flow electrochemical Taylor vortex reactor. *Org. Process Res. Dev.* **2022**, *26*, 2674–2684. [CrossRef] [PubMed]
25. Wilcox, D.C. Reassessment of the scale-determining equation for advanced turbulence models. *AIAA J.* **1988**, *26*, 1299–1310. [CrossRef]
26. Nicoli, A.; Johnson, K.; Jefferson-Loveday, R. Computational modelling of turbulent Taylor–Couette flow for bearing chamber applications: A comparison of unsteady Reynolds-averaged Navier–Stokes models. *Proc. Inst. Mech. Eng. A J. Power Energy.* **2022**, *236*, 985–1005. [CrossRef]
27. Wang, L.; Vigil, R.D.; Fox, R.O. CFD simulation of shear-induced aggregation and breakage in turbulent Taylor-Couette flow. *J. Colloid Interface Sci.* **2005**, *285*, 167–178. [CrossRef] [PubMed]
28. Wereley, S.T.; Lueptow, R.M. Velocity field for Taylor–Couette flow with an axial flow. *Phys. Fluids* **1999**, *11*, 3637–3649. [CrossRef]
29. Koschmieder, E.L. Turbulent Taylor vortex flow. *J. Fluid Mech.* **1979**, *93*, 515–527. [CrossRef]